Mixing characteristics of refractory black carbon aerosols at an urban site in Beijing

Hang Liu[1,2], Xiaole Pan[1], Dantong Liu[3], Xiaoyong Liu[1,4], Xueshun Chen[1], Yu Tian[1], Yele Sun[1,2,4], Pingqing Fu[5], Zifa Wang[1,2,4]

[1] State Key Laboratory of Atmospheric Boundary Layer Physics and Atmospheric Chemistry, Institute of Atmospheric Physics, Chinese Academy of Sciences, Beijing, 100029, China

[2] University of Chinese Academy of Sciences, Beijing, 100049, China

[3] Department of Atmospheric Sciences, School of Earth Sciences, Zhejiang University, Hangzhou, Zhejiang, 310027, China

[4] Center for Excellence in Regional Atmospheric Environment, Chinese Academy of Science, Xiamen, 361021, China

[5] Institute of Surface-Earth System Science, Tianjin University, Tianjin 300072, China

Correspondence to: Xiaole PAN (panxiaole@mail.iap.ac.cn)

Abstract Black carbon aerosols play an important role in climate change because they directly absorb solar radiation. In this study, the mixing state of refractory black carbon (rBC) at an urban site in Beijing in the early summer of 2018 was studied with a single particle soot photometer (SP2) as well as a tandem observation system with a centrifugal particle mass analyzer (CPMA) and a differential mobility analyzer (DMA). The results demonstrated that the mass-equivalent size distribution of rBC exhibited an approximately lognormal distribution with a mass median diameter (MMD) of 171 nm. When the site experienced prevailing southerly winds, the MMD of rBC increased notably, by 19%. During the observational period, the ratio of the diameter of rBC-containing particles (D_p) to the rBC core (D_c) was 1.20 on average for D_c=180 nm, indicating that the majority of rBC particles were thinly coated. The D_p/D_c value exhibited a clear diurnal pattern, with a maximum at 1400 LST and a D_p growth rate of 2.3 nm/h; higher O_x conditions increased the coating growth rate.

The microphysical properties of rBC were also studied. Bare rBC particles were mostly found in fractal structures with a mass fractal dimensions (D_{fm}) of 2.35 with limited variation during both clean and polluted periods. The morphology of rBC changed with coating thickness increasing. When the mass ratio of nonrefractory matter to rBC (M_R) < 1.5, rBC-containing particles were primarily found in external fractal structures and they changed to a core-shell structure when M_R > 6, at which point the measured scattering cross section of rBC-containing particles was consistent with that based on the Mie scattering simulation. We found that only 28% of the rBC-containing particles were in core-shell structures with a particle mass of 10 fg on clean period but that proportion increased considerably, to 45%, on polluted period. Due to the morphology change, the absorption enhancement (E_{abs}) was 12% lower than that predicted for core-shell structures.

1 Introduction

Black carbon (BC) aerosol is one of the principal light-absorbing aerosols in the atmosphere. BC is regarded as one of the most important components contributing to global warming (Bond et al., 2013). BC has a much shorter lifetime than CO_2. Thus, BC's radiative perturbation on a regional scale may be different from globally averaged estimates. It has been reported that BC's direct radiative forcing can reach an order of +10 W m^{-2} over East and South Asia (Bond et al., 2013). BC aerosols can also influence the climate by altering cloud properties, such as the evaporation of cloud droplets, cloud lifetime and albedo (Ramanathan et al., 2001;Ramanathan and Carmichael, 2008). Ding et al. (2016) determined that the existence of BC in the upper mixing layer could absorb downward solar radiation, impeding the development of the boundary layer, which aggravates air pollution. Moreover, BC aerosols have detrimental health effects. Black carbon and organic carbon are regarded as the most toxic pollutants in $PM_{2.5}$ and lead to as many as ~3 million premature deaths worldwide (Adler et al., 2010;Apte et al., 2015).

Black carbon is typically emitted from the incomplete combustion of fossil fuels and biomass. After being emitted into the atmosphere, BC particles tend to mix with other substances through coagulation, condensation, and other photochemical processes that significantly change BC's cloud condensation nuclei activity as well as its light absorption ability (Bond et al., 2013;Liu et al., 2013). The model results suggest that after BC's core is surrounded by a well-mixed shell, its direct absorption radiative forcing could be 50% higher than that of BC in an external mixing structure (Jacobson, 2001). Such an absorption enhancement phenomenon is interpreted as exhibiting a "lensing effect", in which a non-absorbing coating causes more radiation to interact with the BC core and thus more light is absorbed. This absorption enhancement effect has been proven in laboratory studies (Schnaiter et al., 2005). Shiraiwa et al. (2010) reported that the absorption enhancement of BC in a core-shell structure increased with coating thickness and reached a factor as high as 2. Nevertheless, field observation results demonstrated large discrepancies (6 to 40%) in the absorption enhancement of aged BC particles (Cappa et al., 2012;Lack et al., 2012). The discrepancies could be attributed to the complex mixing state of BC in the real atmosphere, which depends on the coating composition, the coating amount and the size of the BC core and structure. Bond et al. (2013) regarded the mixing state of BC as one of the most important uncertainties in evaluating BC direct radiative forcing. Furthermore, freshly emitted BC is initially hydrophobic. Mixing BC with other soluble materials will significantly increase BC-containing particles' hygroscopicity and thus their ability to become cloud condensation nuclei (Bond et al., 2013;Popovicheva et al., 2011). This ability is associated with the wet deposition rate and consequently influences the lifetime and spatial distribution of BC particles in the atmosphere. For these reasons, more observations are needed to determine the specific spatial and temporal distribution of BC's mixing state, which would be helpful for minimizing the uncertainty in evaluating BC's climatic and environmental effects.

China's economy has grown rapidly in recent decades, accompanied by the substantial emission of pollutant precursors. Annual emissions of BC in China are reported to have increased from 0.87 Tg in 1980 to 1.88 Tg in 2009, comprising half of the total emissions in Asia and an average of 18.97% of the global BC emissions during this period (Qin and Xie, 2012). Such

substantial BC emissions greatly influence the regional climate and environment (Ding et al., 2016;Menon et al., 2002).

Although temporal/spatial variations in BC and the corresponding optical properties of aged BC have been recently reported (Cao et al., 2007;Cao et al., 2004;Zhang et al., 2009), the number of observational studies on BC's mixing state remains insufficient. Recently, single particle soot photometer (SP2) has been used as a reliable instrument for estimating the mixing state of BC due to its single particle resolution and high accuracy. Several studies have used SP2 to investigate BC's mixing state in China (Gong et al., 2016;Huang et al., 2012;Wang et al., 2016;Wu et al., 2017). Most studies have primarily focused on the variability of BC's mixing state on severe haze days during winter because of the extremely high concentrations of particle matter and low visibility. In summer, higher radiation and high hydroxyl radical concentrations favor photochemical reactions and thus contribute to the condensation aging of BC. By using a smog chamber, Peng et al. (2016) found that the amount of BC-containing particles increased rapidly owing to the photochemical aging of the BC coating materials from Beijing's urban environment, even in relatively clean conditions. Cheng et al. (2012) noted that the changing rate of BC from an external to internal mixing state can reach up to 20%/ h in summer. Thus, the mixing state of BC should also be carefully considered on relatively clean days during summer.

In this study, we used an SP2 to investigate BC in the urban areas of Beijing, China, during early summer, focusing on the size distribution and coating thickness of BC-containing particles. Field experiments using a tandem system consisting of a centrifugal particle mass analyzer (CPMA, Cambustion Ltd.) and a differential mobility analyzer (DMA, model 3085A, TSI Inc., USA) with an SP2 were performed during two during clean and polluted cases, focusing on BC-containing particles' microphysical properties including the effective density, morphology and light absorption enhancement. The results of this paper were exhibited in the following sequence: (1) the size distribution of BC core and it's influence factors such as seasons, weather condition and etc.; (2) the coating thickness of BC and it's influence factors such as diurnal variation, O_x condition and etc.; (3) the morphology of BC and it's relationship with coating thickness; (4) the relationship of morphology of BC with it's light absorption. Various techniques have been developed to quantify the mass concentration of BC aerosols, including optical, thermal, thermal-optical and photoacoustic methods. For the SP2, the mass concentration of BC was measured on the basis of incandescent signal emissions; therefore, refractory black carbon (rBC) was used. The abbreviations and symbols used in this paper are listed in Table S1.

2 Observation and methodology

2.1 Site description

The measurement of rBC particles was performed from May 30 to June 13, 2018, in an air-conditioned container located in the tower campus of the State Key Laboratory of Atmospheric Boundary Layer Physics and Atmospheric Chemistry, Institute of Atmospheric Physics (LAPC, longitude: 116.37 °E; latitude: 39.97 °N). The sampling site is located between the northern third and fourth ring roads of Beijing, approximately 50 m from the closest road and 380 m away from the nearest highway

95   (the Jingzang highway) (Fig. 1b). Anthropogenic emissions from the experimental campus were negligible. Thus, this site can well represent the urban conditions in Beijing.

2.2 Single-particle soot photometer (SP2)

A single particle soot photometer (SP2, Droplet Measurement Technology, Inc., Boulder, CO, USA) was used to determine the size distribution and mixing state of rBC particles in the atmosphere. In the SP2 measuring chamber, an intense continuous
100   intracavity Nd:YAG laser beam is generated (1064 nm, TEM00 mode). After an rBC-containing particle crosses the beam, it is heated to incandesce by sequentially absorbing the laser power. The maximum incandescence intensity (or the peak height of the incandescence signal) is approximately linearly correlated with rBC mass, irrespective of the presence of non-BC material or the rBC's morphology. The SP2 was calibrated to determine the relationship between the incandescence peak height and the mass of rBC particles using Aquadag aerosols (Acheson Inc., USA). Fig. 2b illustrates the schematic diagram
105   of the calibration system. During calibration, monodisperse Aquadag aerosols were generated with an atomizer (model 3072, TSI Inc., USA) and dried using a diffusion dryer. Then, Aquadag aerosols with known mass (M_{rBC}) were selected with a CPMA and injected into the SP2 to obtain the corresponding laser-induced incandescence (LII) signal. A recent study (Laborde et al., 2012) demonstrated that the mass of rBC particles could be underestimated when using Aquadag aerosol as the calibration material. We performed a correction by multiplying by a factor of 0.75 for LII peak height during the calibration, as described
110   in (Zhang et al., 2018;Liu et al., 2014). The LII peak-M_{rBC} relationship was thus obtained (Fig. S1). The uncertainty of the derived rBC mass was estimated to be 20%, which corresponds to an uncertainty of ~6% of the mass equivalent size (D_c),

$$D_c = \sqrt[3]{\frac{6*M_{rBC}}{\pi*\rho_{rBC}}} \tag{1}$$

by using a 1.8 g cm^{-3} density for rBC material density (Bond et al., 2013).

In addition to the incandescence channel, SP2 also has scattering channels to directly measure the scattering cross section
115   ($\sigma_{measured}$) of every single particle. However, for rBC-containing particles, the particles will evaporate during the measurement since rBC can absorb the laser energy, which results in a decrease in the rBC-containing particles' sizes and thus a decrease in the $\sigma_{measured}$. The leading-edge only (LEO) fitting method was invented to obtain the scattering cross section of the initial rBC-containing particles before evaporation (Gao et al., 2007). With the $\sigma_{measured}$ and D_c, the diameter (D_p) of the rBC-containing particle can be obtained using Mie theory with refractive indices of 2.26-1.26i for the rBC (Moteki et al., 2010) and 1.48-0i
120   for the coatings (Taylor et al., 2015) by assuming a core-shell structure. Thus, the coating thickness of rBC can be directly determined by SP2, as denoted by the shell/core ratio (D_p/D_c). The D_p derivation method based on LEO fitting has been widely used (Taylor et al., 2015;Shiraiwa et al., 2008;Liu et al., 2014;Laborde et al., 2013), and (Liu et al., 2015) estimated that the core-shell assumption will cause <6% uncertainty in the derived D_p/D_c. The scattering signal of SP2 was calibrated using polystyrene latex spheres (PSL, Nanosphere Size Standards, Duke Scientific Corp., USA) with known sizes (203±3 nm: Lot
125   #185856; 303±3 nm: Lot #189903; 400±3 nm: Lot #189904), as shown in Fig. S2. The calibration of the scattering channel and the incandescence channel was also conducted after the observation. The calibration coefficient varied little (<3%) and

the YAG power (laser intensity index recorded by the SP2) fluctuated by 4.8 ± 0.1, indicating the stable condition of the SP2 during the observation period.

The detection efficiency of the SP2 was determined by comparing the number concentrations of Aquadag as simultaneously measured by the SP2 and a condensation particle counter (CPC, model 3775, TSI Inc., USA). For large particles, the SP2 detection efficiency was approximately unity and decreased gradually for smaller rBC particles (Fig. S3). For rBC with $D_c <$ 70 nm, the detection efficiency of the SP2 fell significantly below 60%. The mass concentrations of rBC may be underestimated because of the low detection efficiency of for smaller rBC particles. By extrapolating a lognormal function fit to the observed mass distribution, we found that rBC particles outside the detection range caused an ~15% underestimation of the rBC mass concentration. To compensate, the mass concentration of rBC was corrected by dividing by a factor of 0.85 during the measurement.

In general, the SP2 can directly measure the mass of the rBC core (M_{rBC}) and thus the mass equivalent diameter (D_c). Additionally, the scattering cross section ($\sigma_{measured}$) can be directly obtained by the SP2, and the diameter of the rBC-containing particle (D_p) can be derived using Mie theory.

2.3 Experiment

Two kinds of measurements were conducted in this study: a regular single SP2 observation to provide the number/mass size distribution and coating thickness of the rBC-containing particles and a tandem CPMA/DMA-SP2 experiment to study the microphysical properties of the rBC-containing particles.

2.3.1 Single SP2 measurement

The regular single SP2 observations were conducted from May 30 to June 7 and June 9 to June 12. An aerosol sampling inlet was placed at 4 m above the ground. A PM$_{2.5}$ cyclone (URG-2000-30ENS-1) was used to selectively measure particles with an aerodynamic diameter smaller than 2.5 μm because rBC particles are typically present in the submicron mode. The systematic configuration of the rBC measurements is presented in Fig. 2a. A supporting pump with a flow rate of 9.6 L/min was used to guarantee a total inlet flow rate of 10 L/min (the demanding flow rate of a PM$_{2.5}$ cyclone) and to minimize particle loss in the tube. The residence time of the sampling flow was estimated to be ~17 s. Then, the sample air was dried by passing through a Nafion dryer (MD-700-24S, TSI) at a flow rate of 0.4 lpm. The dried sample was measured with the SP2 and CPC.

2.3.2 Tandem CPMA/DMA-SP2 measurement

The tandem CPMA/DMA-SP2 experiments were conducted on June 8 and 13. June 8 is representative of a clean period, when the concentrations of PM$_{2.5}$ and O$_3$ averaged 20 μg/m^3 and 60 ppbv, respectively. Beijing was mainly affected by a clean northern air mass on June 8 (Fig. S5). June 13 is representative of a polluted period when the hourly mass concentration of PM$_{2.5}$ exceeded 110 μg/m^3; the air mass was from the southern area of Beijing which is one of the most polluted area in China.

Thus, the tandem CPMA/DMA-SP2 experiment was conducted on June 8 and 13 to study the detailed physical characteristics of rBC under different pollution conditions.

As shown in Fig. 2(a), the tandem system was similar to the regular single SP2 observation system. The difference is the neutralizer, and a DMA or CPMA were added in front of the SP2, as denoted by the orange dashed line. Specifically, in the DMA-SP2 system, particles were first selected by DMA to obtain particles with known mobility diameters (D_{mob}). Then, the monodispersed particles were injected into the SP2 to obtain the corresponding information. In practice, we set three D_{mob} setpoints (D_{mob} = 200 nm, 250 nm, 300 nm). The duration of one setpoint is ~20 min, and we recorded data 2 min after we changed the setpoint to allow the system to stabilize. The purpose of the DMA-SP2 system is to obtain the effective density of bare rBC. Bare rBC is defined as rBC with $D_p/D_c \approx 1.0$, and the effective density of bare rBC was calculated according to the following equation:

$$\rho_{eff} = \frac{6M_{rBC}}{\pi D_{mob}^3} \tag{2}$$

In principle, the measured effective density is the same as the material density if the particle has an ideal spherical shape with no void space. Thus, the effective density is an indicator of particle compactness, as it compares the effective density and the material density. Several studies that include the coupling of DMA with APM or CPMA have been conducted to determine the ρ_{eff}-D_{mob} relationship of Aquadag rBC samples in the laboratory (Moteki and Kondo, 2010;Gysel et al., 2011). The relationship between the ρ_{eff} and D_{mob} of Aquadag is presented in Fig. S4. The ρ_{eff} obtained using the DMA-SP2 system in this study agreed well with previous research.

In the CPMA-SP2 system, particles with known mass (M_p) selected by CPMA were injected into the SP2, and the M_p setpoints were 1 fg, 2 fg, 5 fg and 10 fg. The duration of one setpoint was ~20 min, and we waited 2 min after we changed the setpoints to record a measurement. The purpose of the CPMA-SP2 system is to obtain morphological information about rBC-containing particles with different coating degrees. Using a tandem CPMA-SP2 system, the mass of an rBC-containing particle (M_p) and of the rBC core (M_{rBC}) can be simultaneously obtained. The coating thickness can be represented by the mass ratio of the coating to the rBC core ($M_R = (M_p-M_{rBC})/M_{rBC}$) without any assumptions. Knowing M_p and M_{rBC}, the scattering cross section of rBC-containing particles can be calculated through Mie theory with refractive indices of 2.26-1.26i for the rBC and 1.48i for the coatings by assuming a core-shell structure and a coating density of 1.5 g/cm^3. The calculated scattering cross section (σ_{model}) can be compared to the $\sigma_{measured}$ by SP2, which can reflect the morphological characteristic of rBC-containing particles; this comparison will be further discussed in section 4.1.2.

3 Results

3.1 Concentrations of PM$_{2.5}$, rBC and pollutant gases

The temporal variations in the concentrations of PM$_{2.5}$, rBC and gaseous pollutants (O$_3$, NO$_2$) during the project are presented in Fig. 3. The regular pollutant concentrations, including PM$_{2.5}$ (1405-F, ThermoFisher Scientific), NO$_2$ (42c, ThermoFisher Scientific) and O$_3$ (49i, ThermoFisher Scientific), were obtained from a state control air quality site (2.5 km from LAPC), provided by the China National Environmental Monitoring Centre. The mass concentration of PM$_{2.5}$ ranged between 5 and 120 μg/m^3 on a daily basis during the observation period. The mixing ratios of both NO$_2$ and O$_3$ exhibited obvious opposite diurnal variations. The maximum O$_3$ concentration appeared at 1400 LST on June 2 with a value of 145 ppbv, reflecting high atmospheric oxidant levels and strong photochemistry during the observation period. The mass concentration of rBC was 1.2 $\pm$ 0.7 μg/m^3 on average, accounting for 3.5 $\pm$ 2.4% of PM$_{2.5}$ on an hourly basis, which was comparable to the previous filter-based measurement in Beijing, with an average fraction of 3.2% in the summer of 2010 (Zhang et al., 2013). The mass concentration of rBC also exhibited a clear diurnal variation, with a maximum at night and a minimum at noon.

During the period from June 1 to June 6, the meteorological conditions were characterized by low relative humidity (RH < 40%) and strong solar radiation and were favorable for ozone formation. The mixing ratio of ozone was relatively high from June 1 to 6. On June 7, a heavy rainfall event occurred, and most of the major pollutants decreased due to significant wet scavenging. The mass concentration of PM$_{2.5}$ decreased from 65 to 10 μg/m^3, and the mass concentration of rBC decreased from 2.6 to 0.2 μg/m^3 from 0300–0700 LST on June 7. The pollutant concentration remained at a low level from June 7 to 8. After June 9, the ambient RH increased to 80%. Under high humidity conditions, the mass concentration of PM$_{2.5}$ experienced steady growth, increasing from 10 to 120 μg/m^3 and staying at a high level from June 12 to 13. Thus, the tandem DMA/CPMA-SP2 observations were conducted separately on June 8 and June 13, which separately represented the different PM$_{2.5}$ pollution conditions.

3.2 Size distribution of rBC

The number and mass distribution as a function of the D_c are illustrated in Fig. 4. As presented, the number size distribution follows the lognormal distribution and peaks at 70 nm, the mass size distribution is also fitted by the lognormal distribution and the mass median diameter (MMD) was 171 nm during the project. A brief summary of the SP2 observations in China is presented in Table 1. Most previous studies focused on the rBC characteristics in winter when a larger MMD (~200–230 nm) was obtained (Zhang et al., 2013;Wu et al., 2017;Wang et al., 2016;Huang et al., 2012;Gong et al., 2016) than in this study. A similar MMD (180 nm) was reported in urban Shenzhen during a summer observation period (Lan et al., 2013), and a higher MMD (210–222 nm) was reported in winter. Liu et al. (2014) also found a winter-high-summer-low trend for rBC sizes in London, with D_c=149$\pm$22 nm in winter and 120$\pm$6 nm in summer. Laboratory studies have proven that MMD is highly dependent on combustion conditions (Pan et al., 2017) and material. Thus, MMD is a suitable indicator of the sources of rBC. Several studies have suggested that the MMD of rBC from biomass burning and coal is much larger than that from traffic

emissions (Wang et al., 2016;Schwarz et al., 2008). Huang et al. (2012) found the MMD observed at rural sites to be much larger than that observed at urban sites because urban sites are primarily affected by rBC emitted from traffic sources and rural sites are more influenced by rBC from coal combustion. The seasonal trends in MMD may be partially explained by the different rBC sources in summer and winter.

Fig. 5 provides the temporal variations in the mass size distribution of rBC during the entire investigation period. Most rBC particles were within the size range of 70–300 nm, with a clear diurnal pattern of the value of $dM/dlogD_c$. The diurnal cycle reached a peak plateau between 0300–0700 LST and decreased gradually in the afternoon. The cycle was controlled by the combined effects of the development of planetary boundary layer (PBL) variation and on-road rBC emissions.

After the two rain events (June 4 and June 7), the MMD decreased significantly from 186 nm to 170 nm and from 183 nm to 159 nm, respectively, as shown in Fig. 3 and Fig. S7. Taylor et al. (2014) observed that the rBC core size distribution shifted to smaller sizes after a biomass burning plume passed through a precipitating cloud, attributing this shift to the preferential nucleation scavenging of larger rBC cores. By counting the MMD on non-rainy days and rainy days, Wang et al. (2018) also found that the MMD decreased from 164±21 nm to 145±25 nm. The decrease in MMD after rain events can be explained by the preferential wet scavenging of the larger rBC-containing particles.

A pollutant rose plot of MMD versus wind speed and wind direction is presented in Fig. 6a. The MMD of rBC was ~160 nm at low wind speed conditions and exhibited a significant increase with increasing southeast wind speed. The maximum MMD exceeded 190 nm when the wind speed was greater than 10 m/s. Fig. 6b presents the correlation between wind speed and MMD. A southerly wind period was selected when the wind direction was 135–225 °, and a northerly wind period was the time when the wind direction was 325–45 °. The MMD exhibited little correlation with wind speed and varied little between the south and northerly wind periods when the wind speeds were less than 2 m/s, as local rBC emissions were predominant. An MMD of 150–160 nm during low wind speed periods may be characteristic of the local sources. The MMD had a strong positive correlation with the wind speed during the southerly wind period (r^2 =0.93), suggesting that the rBC from the south was larger, which may be the result of the different rBC sources in the southern polluted region. Since the air mass from the north is always clean, the local rBC emissions may be the main contributors to the total rBC concentration in the northerly wind period. Thus, the MMD may be more influenced by local emissions and show a weak correlation with the wind speed during northerly wind periods.

3.3 Temporal variation of D_p/D_c

The D_p/D_c for a given single rBC-containing particle was calculated using the LEO fitting method. Herein, rBC cores with D_c=180 ± 10 nm were selected because the low scattering signal of small rBC is easily influenced by signal noise (D_p/D_c indicates the D_p/D_c with D_c=180 ± 10 nm in the following discussion if not specified). The D_p/D_c variation during the investigation period is illustrated in Fig. 7. In general, D_p/D_c was 1.20±0.05 on average during the investigation, which is consistent with observations (1.15) during the summer in Paris (Laborde et al., 2013). Black carbon sources and the aging process significantly influenced the D_p/D_c of rBC. The rBC from traffic is reported to be relatively uncoated (Liu et al., 2014),

whereas the rBC emitted by biomass burning is found to be moderately coated, with a D_p/D_c=1.20–1.40 (Pan et al., 2017). Moreover, D_p/D_c increases with the aging process, and a larger D_p/D_c (1.60) was found in an aged continental air mass (Shiraiwa et al., 2008). The relatively low D_p/D_c value further supports the argument that rBC was primarily emitted from on-road vehicles during the summer in Beijing.

255 The D_p/D_c distributions for the two episodes before the tandem CPMA/DMA-SP2 experiments are shown in Fig. 7. Episode 1 (June 7 2200 LST – June 8 1200 LST) occurred after a heavy rain period and is representative of clean conditions. Episode 2 (June 11 2300 LST – June 12 1200 LST) was characterized by the highest average D_p/D_c value (1.40) and the highest PM$_{2.5}$ concentration value (120 μg/m^3) during the observation period. The D_p/D_c exhibited a unimodal distribution during episode 1 (Fig. 7b) and a clear bimodal pattern during episode 2 (Fig. 7c) which indicates there may be one type rBC in episode 1 and 260 two types rBC with clear coating thickness difference in episode 2. The coating thickness of the first kind rBC was relatively thin with a D_p/D_c value of ~1.05 corresponding to the single peak of the unimodal distribution in episode 1 and the left peak of the unimodal distribution. This kind rBC may be freshly emitted by the local rBC sources (such as traffic) and underwent a short aging time. However, the second kind of rBC was thickly coated with a D_p/D_c value of ~1.80 corresponding to the right peak of the bimodal distribution during episode 2. Zhang et al. (2018) demonstrated that 63% of the rBC was estimated to be 265 transported from outside of Beijing during previous pollution events, and the rBC-containing particles from regional transportation were characterized by having more coating material. The rBC-containing particles with D_p/D_c = 1.80 in the right peak of the bimodal distribution may be the result of transportation from polluted regions.

3.4 Diurnal variation in D_p/D_c

270 The temporal variation in D_p/D_c exhibited a clear day-high and night-low pattern. Fig. 8 exhibits the diurnal trend of D_p/D_c. The mean D_p/D_c increased during the daytime, with a peak (1.20) at 1400 LST and a minimum (1.12) at 0600 LST. Coating thickness (D_p/D_c) was controlled by the competing effects of emissions and aging because freshly emitted thinly coated rBC tends to decrease D_p/D_c and the aging process tends to increase D_p/D_c. The increasing trend of D_p/D_c during the day could be explained by the prevailing aging process, whereas the decreasing trend at night can be explained by the prevailing emissions 275 process, as the photochemical condensation aging during the day was much faster than the coagulation aging at night (Riemer et al., 2004;Chen et al., 2017). The advection of aged rBC-containing particles from the upper boundary layer with the development of boundary layer during day time may be another reason for the increase of D_p/D_c. By measuring the D_p from 0600–1400 LST, the D_p growth rate was calculated to be 2.3 nm/h. A larger D_p growth rate was found in the period with a high O_x concentration, which may be favorable for the formation of coating material on rBC. The photochemical process and 280 condensation aging have proven to be very efficient during the day. Using a smog chamber, (Peng et al., 2016) found that the D_p growth rate of rBC-containing particles could reach 26 nm/h in Beijing's urban area. Although the photochemical process and condensation may rapidly increase the D_p, the difference between the present study and the smog chamber results indicated

that the "apparent" D_p growth rate in the ambient measurement was relatively low given the continuous freshly emitted rBC in urban Beijing. Thus, the D_p/D_c was always at a low level, resulting in little light absorption enhancement during the summer.

285

4 Discussion

4.1 Morphological evolution of rBC-containing particles

4.1.1 Morphology of bare rBC

By coupling DMA and SP2, the mass and the mobility diameter of bare rBC ($D_p/D_c \approx 1.0$) can be obtained simultaneously,

290 and therefore, the effective density (ρ_{eff}) can be calculated. The ρ_{eff} of the ambient bare rBC was measured on a clean day (June 8) and a polluted day (June 13). The ρ_{eff} of bare rBC at 200–300 nm ranged from 0.41–0.29 g/cm^3, which was much smaller than the material density of rBC (1.8 g/cm^3). This significant discrepancy indicates that bare rBC was in a fractal structure consistent with the previous research from electron microscopic images, which showed that bare rBC was in a fractal chain-like structure (Adachi and Buseck, 2013;Li et al., 2003;Wang et al., 2017). The effective densities showed no evident

295 difference between the pollution day and the clean day because the bare rBC particles were freshly emitted and only affected by local sources. A power law is always used to describe the fractal-like aggregates of particles: $M_p \propto D_{mob}^{Dfm}$ (Moteki and Kondo, 2010;Park et al., 2004), where D_{fm} is defined as the mass fractal dimension that is an indicator of particle compactness. The value of D_{fm} is 3 for ideal spherical particles and less than 3 for fractal particles. Based on the equation for ρ_{eff}, the following relationship can be found: $\rho_{eff} \propto D_{mob}^{Dfm-3}$. Thus, a larger bare rBC had a smaller ρ_{eff}, which was consistent with the

300 results in Fig. 9. A power function was used to fit the observed data. $\rho_{eff} \propto D_{mob}^{-0.65}$ and $\rho_{eff} \propto D_{mob}^{-0.6}$ were found separately on clean and polluted days, corresponding to the mass fractal dimensions of 2.35 and 2.40, respectively. These mass fractal dimensions from the summer in Beijing are similar to the observations (D_{fm}=2.30) from urban Tokyo (Moteki and Kondo, 2010) and the diesel exhaust measurement (D_{fm}=2.35) (Park et al., 2004), suggesting that the freshly emitted bare rBC particles originated primarily from traffic sources. Traffic may contribute a majority of the fresh rBC during both polluted and clean

305 periods in the summer.

4.1.2 Morphology of rBC-containing particles with increasing coating thickness

The morphological characteristics of rBC-containing particles were investigated by comparing the $\sigma_{measured}$ and σ_{model} using a CPMA-SP2 system first proposed by (Liu et al., 2017). The comparison of $\sigma_{measured}$ and σ_{model} as a function of M_R for a particle

310 mass of 10 fg is illustrated in Fig. 10a. If the ratio of $\sigma_{measured}$ and σ_{model} equals 1, it implies that the scattering cross section measured by SP2 is the same as the model prediction under the assumption of a core-shell mixing structure; thus, the rBC-containing particle was likely a core-shell structure. When the rBC was bare ($M_R \approx 0$), the rBC was in a fractal structure, as discussed in section 4.1.1. With increasing M_R, the $\sigma_{measured}/\sigma_{model}$ gradually decreased until M_R=1.5, indicating that the coating material may not be sufficient to encapsulate rBC and that the rBC-containing particles tended not to be away from a core-

shell structure. Liu et al. (2017) showed that rBC-containing particles with $M_R<1.5$ primarily presented an external structure. When $1.5<M_R<6$, the $\sigma_{measured}/\sigma_{model}$ steadily increased, which implied that the shape of rBC-containing particles gradually transformed to become more compact, with a core-shell-like structure, in this stage. When $M_R>6$, the $\sigma_{measured}/\sigma_{model}$ approached 1, indicating that the rBC-containing particles were in a core-shell-like structure in this stage. Similar phenomena were found in the relationship of $\sigma_{measured}/\sigma_{model}$ and M_R for particle masses of 5 fg, as illustrated in Fig. 10b. However, when $M_R \approx 0.1$, the $\sigma_{measured}$ was consistent with the model prediction for a particle mass of 5 fg. This is because the scattering signal was not sensitive to the irregularity of smaller-sized particles (Moteki et al., 2010). Therefore, a Mie theory-based core-shell model could capture the main morphological features.

Different techniques have been used to explore the morphology of rBC-containing particles in ambient and laboratory measurements (Zhang et al., 2008;Peng et al., 2016;Pagels et al., 2009). It is generally agreed that the morphology of rBC-containing particles will become more compact with the aging process or with increasing coating thickness. However, this study reveals that the morphology transform may only be true when the coating is thick enough ($M_R>1.5$), and the coatings may only attach to rBC and slightly influence rBC-containing particles' morphology when the coating is not thick enough ($M_R<1.5$).

Based on the relationship between the $\sigma_{measured}/\sigma_{model}$ and M_R, the rBC-containing particles are classified into three groups: external stage ($0<M_R<1.5$), transit stage ($1.5<M_R<6$) and core-shell stage ($M_R>6$). A similar variation between the $\sigma_{measured}/\sigma_{model}$ and M_R was also found by (Liu et al., 2017;Wu et al., 2018). The M_R transition point from the transit stage and core-shell stage determined by (Liu et al., 2017) is slightly lower than that in this study. Liu et al. (2017) found that the M_R transition point varied among different rBC sources. In addition to rBC sources, the environmental conditions during the aging process of rBC-containing particles, such as temperature and humidity, may also influence the rBC-containing particle morphology. We determined the M_R transition point in Beijing in summer. More work needs to be done in the future to better quantify M_R in different situations.

The combined CPMA and SP2 measurements were conducted separately on a clean day (June 8) and a polluted day (June 13). Fig. 11(a) presents the average M_R for different CPMA setpoints (1 fg, 2 fg, 5 fg, and 10 fg) on June 8 and June 13. The average M_R is 0.77 for M_p =1 fg and 5.29 for M_p =10 fg on the clean day, whereas the average M_R is 0.84 for M_p =1 fg and 7.28 for M_p =10 fg on the pollution day. The average M_R values of the polluted day were all larger than those on the clean day for the four M_p points. This result demonstrated that rBC had more coating material on the polluted day than on the clean day. Based on the M_R transition points discussed above, the rBC-containing particles were classified into three stages as shown in Fig. 11(b). The rBC-containing particles with $M_p=1$ fg were primarily in the external mixing stage regardless of the pollution conditions. With an increase in M_p, more rBC-containing particles were in the transition or core-shell stage. On the clean day, 28% of the rBC-containing particles were in the core-shell stage, when $M_p=10$ fg. However, on the pollution day, 45% of the rBC-containing particles were in the core-shell stage, when $M_p=10$ fg. This phenomenon implied that most rBC-containing particles are not in an ideal core-shell structure on clean days, whereas more rBC-containing particles were in a core-shell structure with thicker coatings on the pollution day.

4.2 Implications of rBC-containing particle morphology for light absorption

350   The morphology of rBC-containing particles varied with M_R. A simple core-shell model, as always used in the previous research to determine optical properties, will certainly cause bias. Based on the classification of the rBC-containing particles according to the relationship between $\sigma_{measured}/\sigma_{model}$ and M_R, Liu et al. (2017) proposed a simple morphology-dependent scheme in which the rBC-containing particles at the external stage were considered to have no absorption enhancement (E_{abs}) and the rBC-containing particles at the core-shell stage were considered to have the same E_{abs} from Mie theory under the

355   assumption of a perfect core-shell structure. The E_{abs} at the transit stage was calculated by the interpolation of E_{abs} between the external and core-shell stages. A graphical and detailed description of the calculation of E_{abs} can be found in Fig. S6. Liu et al. (2017) proved that this morphology-dependent scheme is in good agreement with the measured E_{abs}. Thus, the E_{abs} at 550 nm wavelength with D_c=180±10 nm was calculated separately using the core-shell model and the morphology-dependent scheme to quantify the uncertainty of using a core-shell model, as shown in Fig. 12. The absorption enhancement was 1.15, on average,

360   using the core-shell model but was only 1.03 using the new scheme. The E_{abs} determined by the core-shell model was overestimated 12% because the observed averaged coating thickness (D_p/D_c=1.2) determined from single SP2 measurements corresponded to M_R=0.37, suggesting that the coating material was not sufficient and most of the rBC-containing particles were not in a core-shell structure in summer in Beijing. Thus, it is necessary to consider the morphology of rBC-containing particles when calculating their optical properties.

365   **5 Conclusion**

The mixing characteristics of rBC-containing particles were investigated in Beijing during the early summer of 2018 using a single particle soot photometer (SP2). The rBC had an approximately log-normal distribution as a function of the mass equivalent diameter (D_c), characterized by a mass median diameter (MMD) of 171 nm, which is consistent with previous urban measurements. The mass size distribution was highly associated with the meteorological conditions. Heavy rain events caused

370   the rBC mass size distribution to be smaller, indicating that wet scavenging may be a more efficient removal mechanism for larger rBC-containing particles. The mass size distribution of rBC shifted to larger sizes when southerly winds prevailed, which was primarily caused by the different rBC sources in the south.

The D_p/D_c was 1.20 on average, with D_c=180 nm during the investigation period, indicating a low coating thickness of rBC during the summer. The coating thickness exhibited a clear diurnal pattern with a peak at 1400 LST, increasing from 0600 to

375   1400 LST at a D_p growth rate of 2.3 nm/h, with D_c=180 nm during the day. The growth rate was much higher in high O_x periods. However, this growth rate was significantly lower than that in the smog chamber results, with a growth rate of 26 nm/h, because the continuously emitted fresh rBC lowered the D_p/D_c in ambient measurements. Although photochemical aging may be very efficient, with continuously emitted fresh rBC, the D_p/D_c increase in the ambient air was very slow, indicating that the rBC-containing particles were primarily at a low D_p/D_c level in summer.

A tandem measurement system with a differential mobility analyzer (DMA) and a centrifugal particle mass analyzer (CPMA) were coupled with an SP2 to investigate the detailed characteristics of rBC-containing particles in summer. The results showed that the effective density of bare rBC ($D_p/D_c=1.0$) was determined to be 0.41–0.30 g/cm^3 for D_c=200–300 nm. These effective densities were significantly lower than the rBC material density (1.8 g/cm^3), suggesting that the bare rBC was in a fractal structure. The corresponding mass fractal dimension (D_{fm}) was 2.35, which agrees well with the D_{fm} of the direct measurement from vehicles, and was unchanged regardless of pollution, indicating that traffic emissions are a major source of fresh bare rBC on both clean and polluted days during the summer in Beijing. With increasing coating thickness, the morphology of rBC changed from a fractal structure to a compact core-shell structure. When M_R (M_{coat}/M_{rBC}) <1.5, rBC-containing particles were in an external structure. When M_R>6, rBC-containing particles were in a core-shell structure. When 1.5<M_R<6, the rBC-containing particles were in a transition stage.

Based on the core-shell model and Mie theory, a new morphology-dependent absorption enhancement (E_{abs}) scheme was proposed and applied to the ambient measurements. A simulation showed that the E_{abs} averaged 1.03 with D_c=180 nm at a wavelength of 550 nm in the summer. The core-shell model overestimated the E_{abs} by 12%.

Data availability

To request the data given in this study, please contact Dr. Xiaole Pan at the Institute of Atmospheric Physics, Chinese Academy of Sciences, via email (panxiaole@mail.iap.ac.cn).

Author contributions

H. L and X. P designed the research; H. L, X. P, X. L, Y. T, Y. S, P. F, and Z. W performed the experiments; H. L, X. P, D. L, and X. C performed the data analysis; H. L and X. P wrote the paper.

Competing interests

The authors declare that they have no conflict of interest.

Acknowledgements

This study was supported by the National Natural Science Foundation of China (grant No. 41877314, 41675128).

Reference

Adachi, K., and Buseck, P. R.: Changes of ns-soot mixing states and shapes in an urban area during CalNex, J. Geophys. Res.-

Atmos., 118, 3723-3730, 10.1002/jgrd.50321, 2013.

Adler, G., Riziq, A. A., Erlick, C., and Rudich, Y.: Effect of intrinsic organic carbon on the optical properties of fresh diesel soot, P Natl Acad Sci USA, 107, 6699-6704, 10.1073/pnas.0903311106, 2010.

410   Apte, J. S., Marshall, J. D., Cohen, A. J., and Brauer, M.: Addressing Global Mortality from Ambient PM2.5, Environ Sci Technol, 49, 8057-8066, 10.1021/acs.est.5b01236, 2015.

Bond, T. C., Doherty, S. J., Fahey, D., Forster, P., Berntsen, T., DeAngelo, B., Flanner, M., Ghan, S., Kärcher, B., and Koch, D.: Bounding the role of black carbon in the climate system: A scientific assessment, Journal of Geophysical Research: Atmospheres, 118, 5380-5552, 2013.

Cao, J. J., Lee, S. C., Ho, K. F., Zou, S. C., Fung, K., Li, Y., Watson, J. G., and Chow, J. C.: Spatial and seasonal variations of 415   atmospheric organic carbon and elemental carbon in Pearl River Delta Region, China, Atmos Environ, 38, 4447-4456, 10.1016/j.atmosenv.2004.05.016, 2004.

Cao, J. J., Lee, S. C., Chow, J. C., Watson, J. G., Ho, K. F., Zhang, R. J., Jin, Z. D., Shen, Z. X., Chen, G. C., Kang, Y. M., Zou, S. C., Zhang, L. Z., Qi, S. H., Dai, M. H., Cheng, Y., and Hu, K.: Spatial and seasonal distributions of carbonaceous aerosols over China, J. Geophys. Res.-Atmos., 112, Artn D22s1110.1029/2006jd008205, 2007.

420   Cappa, C. D., Onasch, T. B., Massoli, P., Worsnop, D. R., Bates, T. S., Cross, E. S., Davidovits, P., Hakala, J., Hayden, K. L., Jobson, B. T., Kolesar, K. R., Lack, D. A., Lerner, B. M., Li, S. M., Mellon, D., Nuaaman, I., Olfert, J. S., Petaja, T., Quinn, P. K., Song, C., Subramanian, R., Williams, E. J., and Zaveri, R. A.: Radiative Absorption Enhancements Due to the Mixing State of Atmospheric Black Carbon, Science, 337, 1078-1081, 10.1126/science.1223447, 2012.

Chen, X. S., Wang, Z. F., Yu, F. Q., Pan, X. L., Li, J., Ge, B. Z., Wang, Z., Hu, M., Yang, W. Y., and Chen, H. S.: Estimation 425   of atmospheric aging time of black carbon particles in the polluted atmosphere over central-eastern China using microphysical process analysis in regional chemical transport model, Atmos Environ, 163, 44-56, 10.1016/j.atmosenv.2017.05.016, 2017.

Cheng, Y. F., Su, H., Rose, D., Gunthe, S. S., Berghof, M., Wehner, B., Achtert, P., Nowak, A., Takegawa, N., Kondo, Y., Shiraiwa, M., Gong, Y. G., Shao, M., Hu, M., Zhu, T., Zhang, Y. H., Carmichael, G. R., Wiedensohler, A., Andreae, M. O., and Poschl, U.: Size-resolved measurement of the mixing state of soot in the megacity Beijing, China: diurnal cycle, aging and 430   parameterization, Atmospheric Chemistry and Physics, 12, 4477-4491, 10.5194/acp-12-4477-2012, 2012.

Ding, A. J., Huang, X., Nie, W., Sun, J. N., Kerminen, V. M., Petaja, T., Su, H., Cheng, Y. F., Yang, X. Q., Wang, M. H., Chi, X. G., Wang, J. P., Virkkula, A., Guo, W. D., Yuan, J., Wang, S. Y., Zhang, R. J., Wu, Y. F., Song, Y., Zhu, T., Zilitinkevich, S., Kulmala, M., and Fu, C. B.: Enhanced haze pollution by black carbon in megacities in China, Geophysical Research Letters, 43, 2873-2879, 10.1002/2016gl067745, 2016.

435   Gao, R. S., Schwarz, J. P., Kelly, K. K., Fahey, D. W., Watts, L. A., Thompson, T. L., Spackman, J. R., Slowik, J. G., Cross, E. S., Han, J. H., Davidovits, P., Onasch, T. B., and Worsnop, D. R.: A novel method for estimating light-scattering properties of soot aerosols using a modified single-particle soot photometer, Aerosol Science and Technology, 41, 125-135, 10.1080/02786820601118398, 2007.

Gong, X. D., Zhang, C., Chen, H., Nizkorodov, S. A., Chen, J. M., and Yang, X.: Size distribution and mixing state of black 440   carbon particles during a heavy air pollution episode in Shanghai, Atmospheric Chemistry and Physics, 16, 5399-5411, 10.5194/acp-16-5399-2016, 2016.

Gysel, M., Laborde, M., Olfert, J. S., Subramanian, R., and Grohn, A. J.: Effective density of Aquadag and fullerene soot black carbon reference materials used for SP2 calibration, Atmos Meas Tech, 4, 2851-2858, 10.5194/amt-4-2851-2011, 2011.

Huang, X. F., Sun, T. L., Zeng, L. W., Yu, G. H., and Luan, S. J.: Black carbon aerosol characterization in a coastal city in 445   South China using a single particle soot photometer, Atmos Environ, 51, 21-28, 10.1016/j.atmosenv.2012.01.056, 2012.

Jacobson, M. Z.: Strong radiative heating due to the mixing state of black carbon in atmospheric aerosols, Nature, 409, 695-697, Doi 10.1038/35055518, 2001.

Laborde, M., Mertes, P., Zieger, P., Dommen, J., Baltensperger, U., and Gysel, M.: Sensitivity of the Single Particle Soot Photometer to different black carbon types, Atmos Meas Tech, 5, 1031-1043, 10.5194/amt-5-1031-2012, 2012.

450   Laborde, M., Crippa, M., Tritscher, T., Juranyi, Z., Decarlo, P. F., Temime-Roussel, B., Marchand, N., Eckhardt, S., Stohl, A., Baltensperger, U., Prevot, A. S. H., Weingartner, E., and Gysel, M.: Black carbon physical properties and mixing state in the European megacity Paris, Atmospheric Chemistry and Physics, 13, 5831-5856, 10.5194/acp-13-5831-2013, 2013.

Lack, D. A., Langridge, J. M., Bahreini, R., Cappa, C. D., Middlebrook, A. M., and Schwarz, J. P.: Brown carbon and internal mixing in biomass burning particles, P Natl Acad Sci USA, 109, 14802-14807, 10.1073/pnas.1206575109, 2012.

455   Lan, Z. J., Huang, X. F., Yu, K. Y., Sun, T. L., Zeng, L. W., and Hu, M.: Light absorption of black carbon aerosol and its

enhancement by mixing state in an urban atmosphere in South China, Atmos Environ, 69, 118-123, 10.1016/j.atmosenv.2012.12.009, 2013.

Li, J., Posfai, M., Hobbs, P. V., and Buseck, P. R.: Individual aerosol particles from biomass burning in southern Africa: 2, Compositions and aging of inorganic particles, J. Geophys. Res.-Atmos., 108, 2003.

460   Liu, D., Allan, J., Whitehead, J., Young, D., Flynn, M., Coe, H., McFiggans, G., Fleming, Z. L., and Bandy, B.: Ambient black carbon particle hygroscopic properties controlled by mixing state and composition, Atmospheric Chemistry and Physics, 13, 2015-2029, 10.5194/acp-13-2015-2013, 2013.

Liu, D., Allan, J. D., Young, D. E., Coe, H., Beddows, D., Fleming, Z. L., Flynn, M. J., Gallagher, M. W., Harrison, R. M., Lee, J., Prevot, A. S. H., Taylor, J. W., Yin, J., Williams, P. I., and Zotter, P.: Size distribution, mixing state and source
465   apportionment of black carbon aerosol in London during wintertime, Atmospheric Chemistry and Physics, 14, 10061-10084, 10.5194/acp-14-10061-2014, 2014.

Liu, D. T., Taylor, J. W., Young, D. E., Flynn, M. J., Coe, H., and Allan, J. D.: The effect of complex black carbon microphysics on the determination of the optical properties of brown carbon, Geophysical Research Letters, 42, 613-619, 10.1002/2014gl062443, 2015.

470   Liu, D. T., Whitehead, J., Alfarra, M. R., Reyes-Villegas, E., Spracklen, D. V., Reddington, C. L., Kong, S. F., Williams, P. I., Ting, Y. C., Haslett, S., Taylor, J. W., Flynn, M. J., Morgan, W. T., McFiggans, G., Coe, H., and Allan, J. D.: Black-carbon absorption enhancement in the atmosphere determined by particle mixing state, Nat Geosci, 10, 184-U132, 10.1038/Ngeo2901, 2017.

Menon, S., Hansen, J., Nazarenko, L., and Luo, Y.: Climate effects of black carbon aerosols in China and India, Science, 297,
475   2250-2253, 2002.

Moteki, N., and Kondo, Y.: Dependence of Laser-Induced Incandescence on Physical Properties of Black Carbon Aerosols: Measurements and Theoretical Interpretation, Aerosol Science and Technology, 44, 663-675, Pii 924375405 10.1080/02786826.2010.484450, 2010.

Moteki, N., Kondo, Y., and Nakamura, S.: Method to measure refractive indices of small nonspherical particles: Application
480   to black carbon particles, J Aerosol Sci, 41, 513-521, 10.1016/j.jaerosci.2010.02.013, 2010.

Pagels, J., Khalizov, A. F., McMurry, P. H., and Zhang, R. Y.: Processing of Soot by Controlled Sulphuric Acid and Water CondensationMass and Mobility Relationship, Aerosol Science and Technology, 43, 629-640, Pii 910341827 10.1080/02786820902810685, 2009.

Pan, X. L., Kanaya, Y., Taketani, F., Miyakawa, T., Inomata, S., Komazaki, Y., Tanimoto, H., Wang, Z., Uno, I., and Wang, Z.
485   F.: Emission characteristics of refractory black carbon aerosols from fresh biomass burning: a perspective from laboratory experiments, Atmospheric Chemistry and Physics, 17, 13001-13016, 10.5194/acp-17-13001-2017, 2017.

Park, K., Kittelson, D. B., and McMurry, P. H.: Structural properties of diesel exhaust particles measured by transmission electron microscopy (TEM): Relationships to particle mass and mobility, Aerosol Science and Technology, 38, 881-889, 10.1080/027868290505189, 2004.

490   Peng, J. F., Hu, M., Guo, S., Du, Z. F., Zheng, J., Shang, D. J., Zamora, M. L., Zeng, L. M., Shao, M., Wu, Y. S., Zheng, J., Wang, Y., Glen, C. R., Collins, D. R., Molina, M. J., and Zhang, R. Y.: Markedly enhanced absorption and direct radiative forcing of black carbon under polluted urban environments, P Natl Acad Sci USA, 113, 4266-4271, 10.1073/pnas.1602310113, 2016.

Popovicheva, O. B., Persiantseva, N. M., Kireeva, E. D., Khokhlova, T. D., and Shonija, N. K.: Quantification of the
495   Hygroscopic Effect of Soot Aging in the Atmosphere: Laboratory Simulations, J Phys Chem A, 115, 298-306, 10.1021/jp109238x, 2011.

Qin, Y., and Xie, S. D.: Spatial and temporal variation of anthropogenic black carbon emissions in China for the period 1980-2009, Atmospheric Chemistry and Physics, 12, 4825-4841, 10.5194/acp-12-4825-2012, 2012.

Ramanathan, V., Crutzen, P. J., Kiehl, J. T., and Rosenfeld, D.: Atmosphere - Aerosols, climate, and the hydrological cycle,
500   Science, 294, 2119-2124, DOI 10.1126/science.1064034, 2001.

Ramanathan, V., and Carmichael, G.: Global and regional climate changes due to black carbon, Nat Geosci, 36, págs. 335-358, 2008.

Riemer, N., Vogel, H., and Vogel, B.: Soot aging time scales in polluted regions during day and night, Atmospheric Chemistry and Physics, 4, 1885-1893, DOI 10.5194/acp-4-1885-2004, 2004.

505   Schnaiter, M., Linke, C., Möhler, O., Naumann, K. H., Saathoff, H., Wagner, R., Schurath, U., and Wehner, B.: Absorption

amplification of black carbon internally mixed with secondary organic aerosol, Journal of Geophysical Research Atmospheres, 110, -, 2005.

Schwarz, J. P., Gao, R. S., Spackman, J. R., Watts, L. A., Thomson, D. S., Fahey, D. W., Ryerson, T. B., Peischl, J., Holloway, J. S., Trainer, M., Frost, G. J., Baynard, T., Lack, D. A., de Gouw, J. A., Warneke, C., and Del Negro, L. A.: Measurement of the mixing state, mass, and optical size of individual black carbon particles in urban and biomass burning emissions, Geophysical Research Letters, 35, Artn L1381010.1029/2008gl033968, 2008.

Shiraiwa, M., Kondo, Y., Moteki, N., Takegawa, N., Sahu, L., Takami, A., Hatakeyama, S., Yonemura, S., and Blake, D.: Radiative impact of mixing state of black carbon aerosol in Asian outflow, Journal of Geophysical Research: Atmospheres, 113, 2008.

Shiraiwa, M., Kondo, Y., Iwamoto, T., and Kita, K.: Amplification of Light Absorption of Black Carbon by Organic Coating, Aerosol Science and Technology, 44, 46-54, 10.1080/02786820903357686, 2010.

Taylor, J. W., Allan, J. D., Allen, G., Coe, H., Williams, P. I., Flynn, M. J., Le Breton, M., Muller, J. B. A., Percival, C. J., Oram, D., Forster, G., Lee, J. D., Rickard, A. R., Parrington, M., and Palmer, P. I.: Size-dependent wet removal of black carbon in Canadian biomass burning plumes, Atmospheric Chemistry and Physics, 14, 13755-13771, 10.5194/acp-14-13755-2014, 2014.

Taylor, J. W., Allan, J. D., Liu, D., Flynn, M., Weber, R., Zhang, X., Lefer, B. L., Grossberg, N., Flynn, J., and Coe, H.: Assessment of the sensitivity of core/shell parameters derived using the single-particle soot photometer to density and refractive index, Atmos Meas Tech, 8, 1701-1718, 10.5194/amt-8-1701-2015, 2015.

Wang, Q. Y., Huang, R. J., Zhao, Z. Z., Cao, J. J., Ni, H. Y., Tie, X. X., Zhao, S. Y., Su, X. L., Han, Y. M., Shen, Z. X., Wang, Y. C., Zhang, N. N., Zhou, Y. Q., and Corbin, J. C.: Physicochemical characteristics of black carbon aerosol and its radiative impact in a polluted urban area of China, J. Geophys. Res.-Atmos., 121, 12505-12519, 10.1002/2016jd024748, 2016.

Wang, Q. Y., Cao, J. J., Han, Y. M., Tian, J., Zhu, C. S., Zhang, Y. G., Zhang, N. N., Shen, Z. X., Ni, H. Y., Zhao, S. Y., and Wu, J. R.: Sources and physicochemical characteristics of black carbon aerosol from the southeastern Tibetan Plateau: internal mixing enhances light absorption, Atmospheric Chemistry and Physics, 18, 4639-4656, 10.5194/acp-18-4639-2018, 2018.

Wang, Y. Y., Liu, F. S., He, C. L., Bi, L., Cheng, T. H., Wang, Z. L., Zhang, H., Zhang, X. Y., Shi, Z. B., and Li, W. J.: Fractal Dimensions and Mixing Structures of Soot Particles during Atmospheric Processing, Environ Sci Tech Let, 4, 487-493, 10.1021/acs.estlett.7b00418, 2017.

Wu, Y., Cheng, T. H., Liu, D. T., Allan, J. D., Zheng, L. J., and Chen, H.: Light Absorption Enhancement of Black Carbon Aerosol Constrained by Particle Morphology, Environ Sci Technol, 52, 6912-6919, 10.1021/acs.est.8b00636, 2018.

Wu, Y. F., Wang, X. J., Tao, J., Huang, R. J., Tian, P., Cao, J. J., Zhang, L. M., Ho, K. F., Han, Z. W., and Zhang, R. J.: Size distribution and source of black carbon aerosol in urban Beijing during winter haze episodes, Atmospheric Chemistry and Physics, 17, 7965-7975, 10.5194/acp-17-7965-2017, 2017.

Zhang, R., Jing, J., Tao, J., Hsu, S. C., Wang, G., Cao, J., Lee, C. S. L., Zhu, L., Chen, Z., Zhao, Y., and Shen, Z.: Chemical characterization and source apportionment of PM2.5 in Beijing: seasonal perspective, Atmospheric Chemistry and Physics, 13, 7053-7074, 10.5194/acp-13-7053-2013, 2013.

Zhang, R. J., Ho, K. F., Cao, J. J., Han, Z. W., Zhang, M. G., Cheng, Y., and Lee, S. C.: Organic carbon and elemental carbon associated with PM10 in Beijing during spring time, J Hazard Mater, 172, 970-977, 10.1016/j.jhazmat.2009.07.087, 2009.

Zhang, R. Y., Khalizov, A. F., Pagels, J., Zhang, D., Xue, H. X., and McMurry, P. H.: Variability in morphology, hygroscopicity, and optical properties of soot aerosols during atmospheric processing, P Natl Acad Sci USA, 105, 10291-10296, 10.1073/pnas.0804860105, 2008.

Zhang, Y. X., Zhang, Q., Cheng, Y. F., Su, H., Li, H. Y., Li, M., Zhang, X., Ding, A. J., and He, K. B.: Amplification of light absorption of black carbon associated with air pollution, Atmospheric Chemistry and Physics, 18, 9879-9896, 10.5194/acp-18-9879-2018, 2018.

Table 1. Brief summary of some of the observations on the mixing state of rBC-containing particles.

rBC type	Site	Period	MMD (nm)	D_p/D_c	Description	Reference
Urban emissions (UE)	Shenzhen, China	Aug–Sep (summer)	180*		The measurement station was on a university campus located in the urban area of Shenzhen.	(Lan et al., 2013)
	Shenzhen, China	Jan–Feb (winter)	210*		The measurement station was the same as the above site.	(Huang et al., 2012)
	Shanghai, China	Dec (winter)	200	2–8	The maximum $PM_{2.5}$ mass loading reached 636 μg/m³.	(Gong et al., 2016)
	Beijing, China	Feb–Mar (winter)	213		The same measurement site as this study.	(Wu et al., 2017)
	This study	Jun (summer)	171	1.20 (D_c=180 nm)		
	London, United Kingdom	Jan–Feb (winter)	149	1.2–2 (D_c=110–150 nm)	During the Clean Air for London (ClearfLo) project.	(Liu et al., 2014)
		Jul–Aug (summer)	120			
Biomass burning (BB)	Airborne measurements	Sep (autumn)	210	1.33 (D_c=190–210 nm)	The MMD and D_p/D_c were both higher for BB than UE.	(Schwarz et al., 2008)
			189	1.2–1.4 (D_c=200 nm)	Fresh, laboratory-produced biomass burning rBC.	(Pan et al., 2017)
	Airborne measurements	Jul–Aug (summer)	195	2.35 (D_c=130–230 nm)	During the second phase of the BORTAS project.	(Taylor et al., 2014)

* Assuming the density of rBC is 2 g/cm³

555
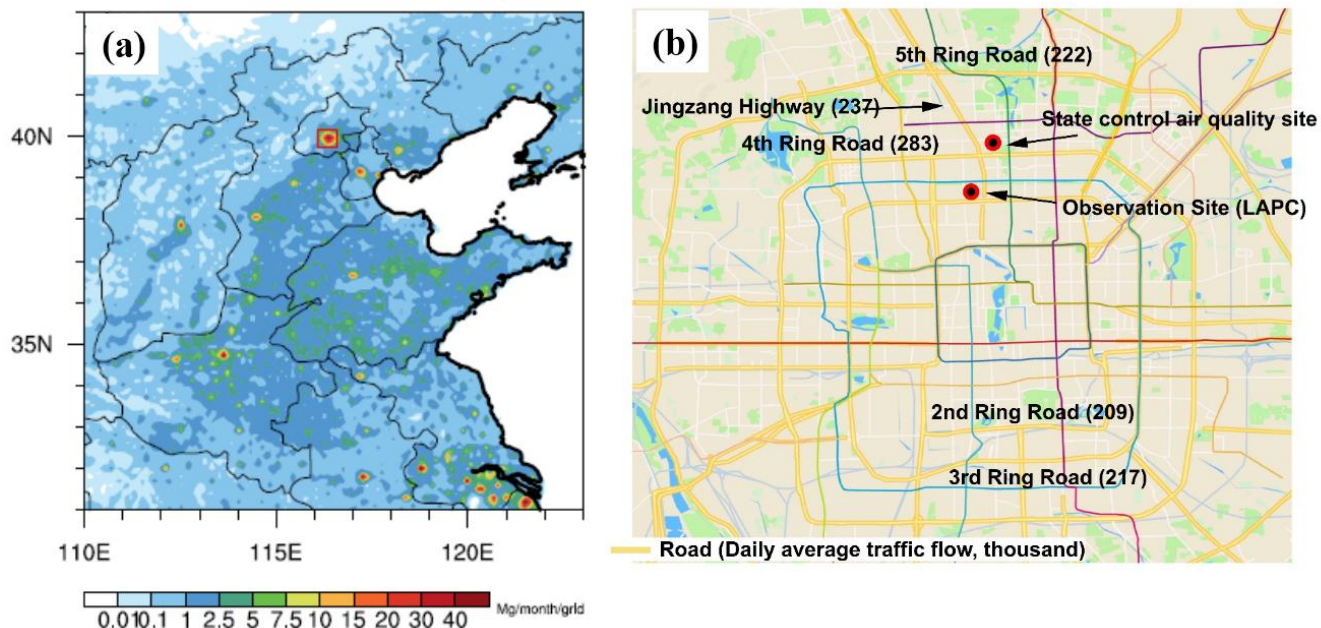
Figure 1. (a) Monthly emissions of BC from traffic in June in east-central China. The red box denotes the geographical location of the observation site, the map is extracted from NCL software (© 2019 NCL, www.ncl.ucar.edu). (b) Road map and traffic flow rate of Beijing. The red circle denotes the observation site, the map is extracted from google map (© 2019 Google, www.google.com/maps).
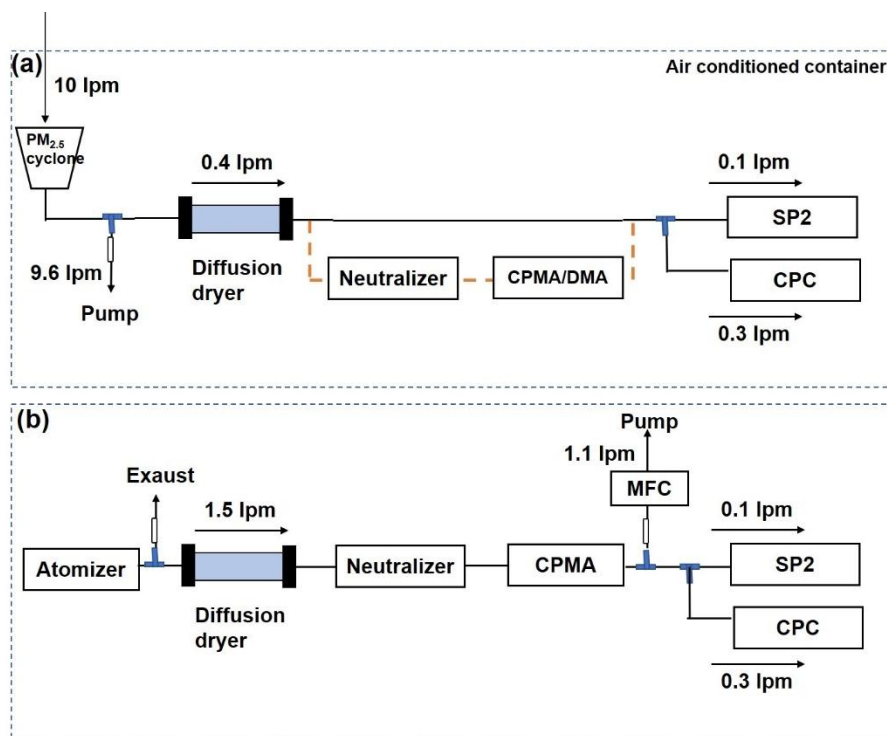
Figure 2. Schematic diagram of (a) the measurement system, with the orange dashed line denoting the tandem CPMA/DMA-SP2 measurement system, during the periods June 9 and 13, and (b) the calibration system.
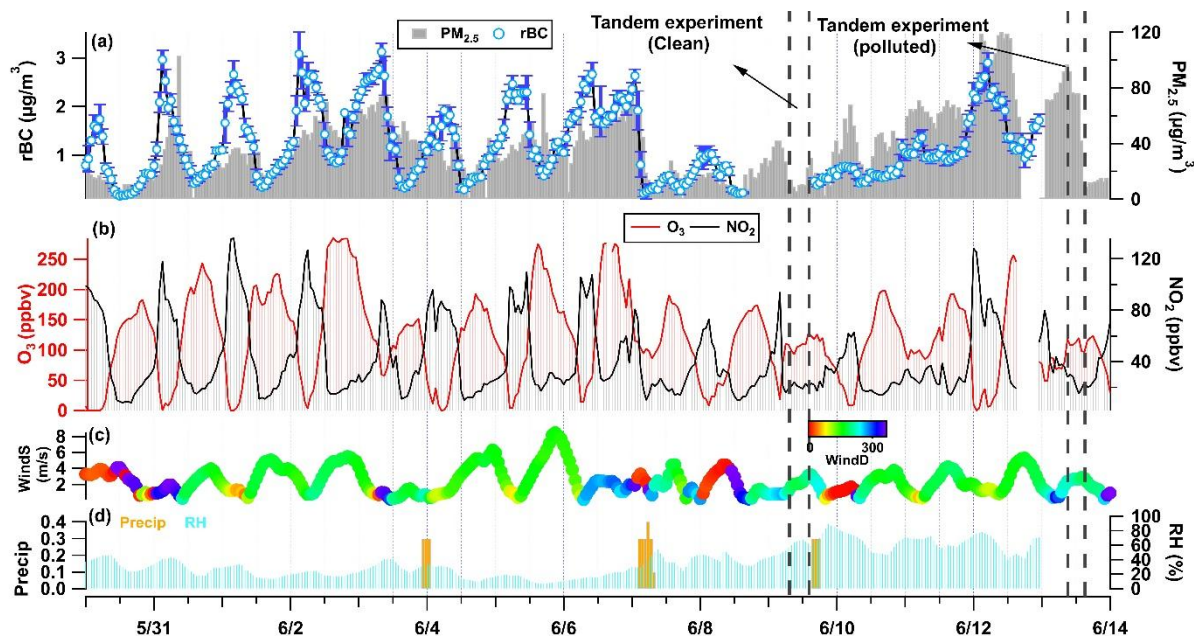
Figure 3. Time series of aerosol/gaseous pollutants and meteorological conditions during the observation period.
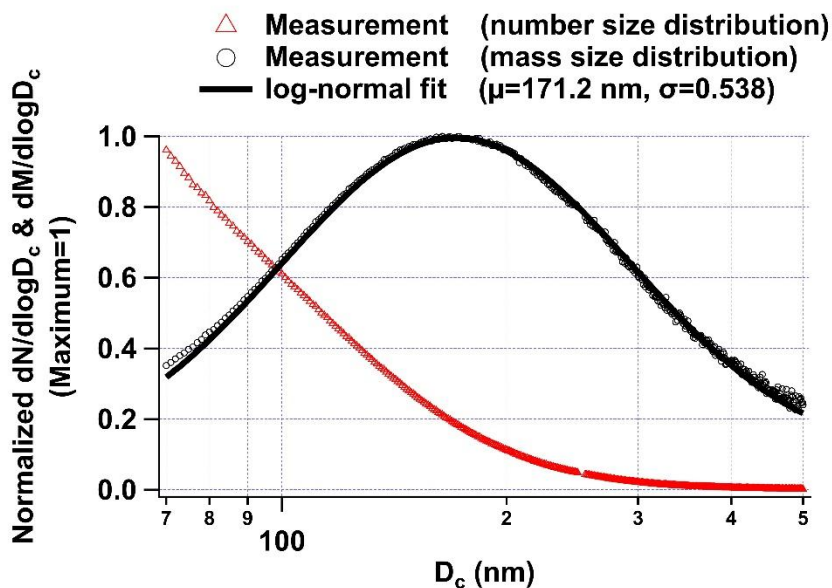
Figure 4. Number and mass size distribution (dN/dlogD_c & dM/dlogD_c) during the observation period.
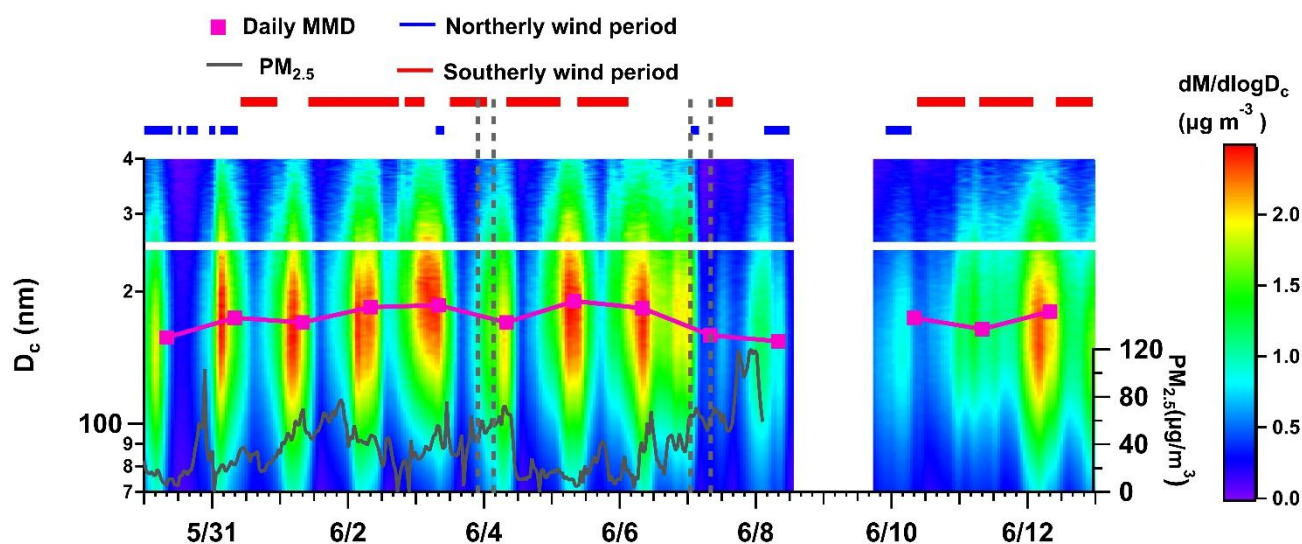
Figure 5. Time series of the mass size distribution of rBC. A southerly wind period is selected when the wind direction is 135–225 ° and a northerly wind period is the time when the wind direction is 325–45 °. The gray dashed line denotes the rainy period.
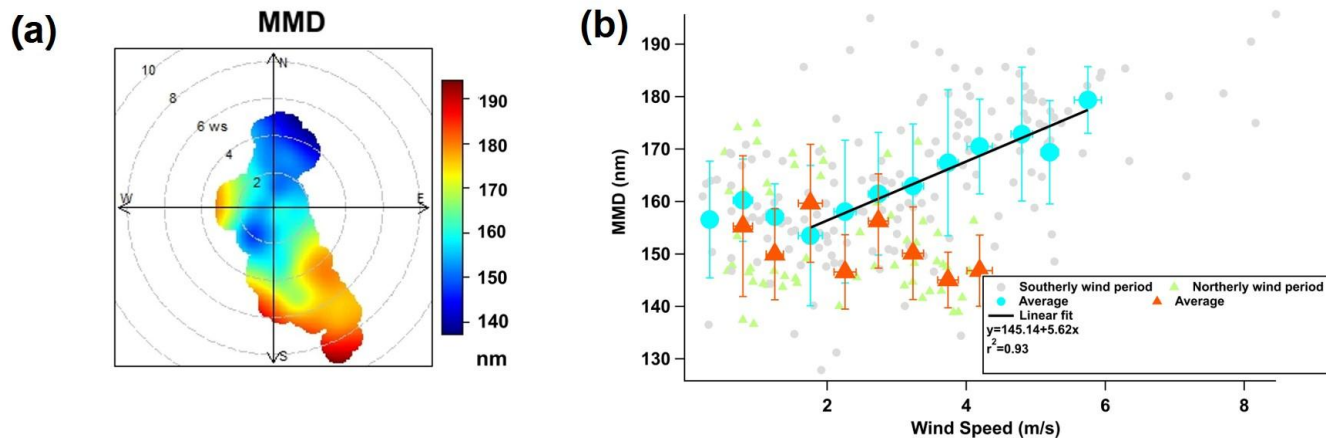
Figure 6. (a) Dependence of rBC's MMD on wind speed and wind direction during the observation period. (b) MMD versus wind speed during the southerly wind period and northerly wind period. The error bars correspond to the standard deviations of MMD in each wind speed bin.
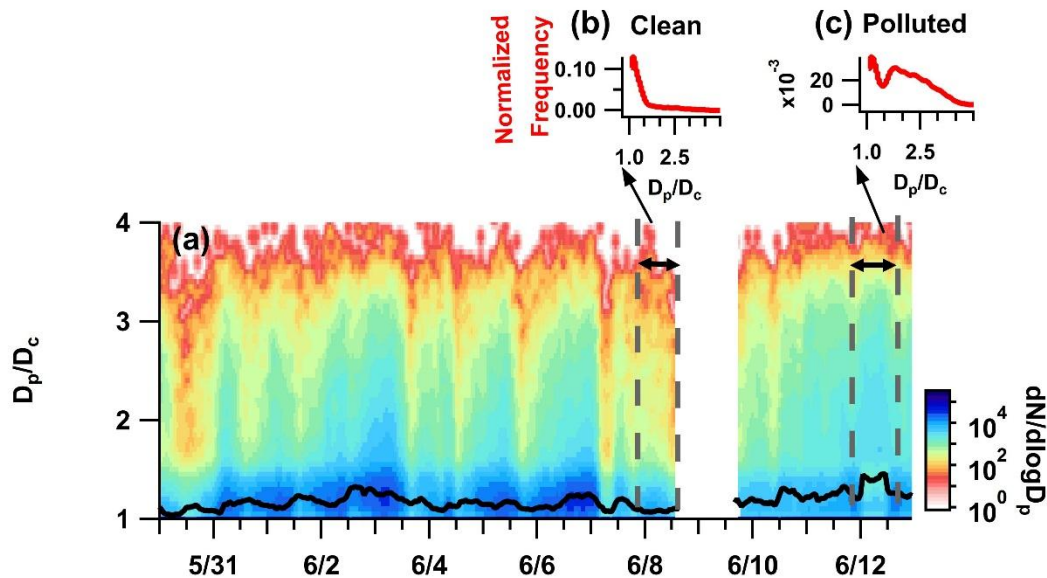
Figure 7. (a) Temporal variation in D_p/D_c, with D_c=180 nm, the image plot denotes the frequency (dN/dlogD_p) of rBC-containing particles with varied D_p/D_c. The black line denotes the average D_p/D_c for each hour. **(b)** The normalized frequency of D_p/D_c for the clean period before the tandem experiment. **(c)** The normalized frequency of D_p/D_c for the polluted period.

585
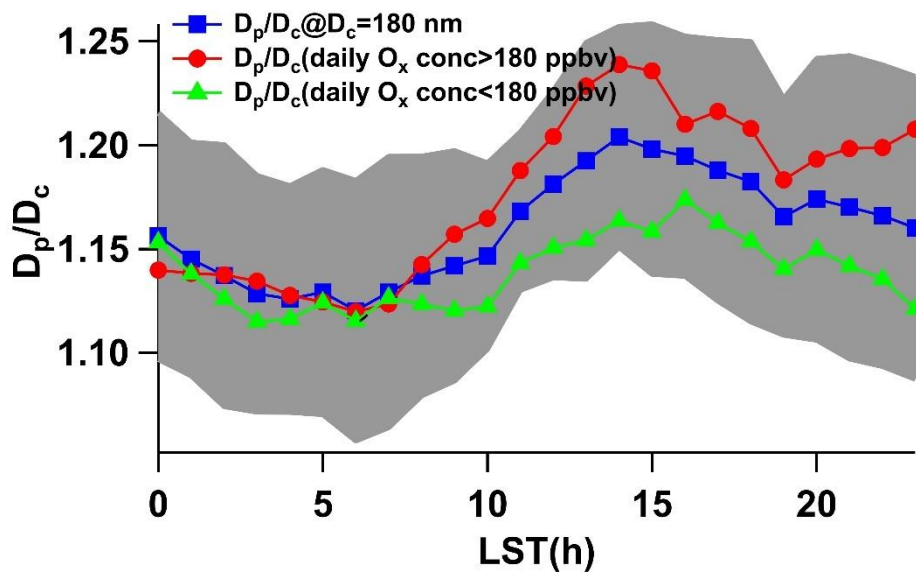
Figure 8. Diurnal variation in D_p/D_c for all periods, high O_x periods and low O_x periods. The gray shaded area denotes the standard deviation of D_p/D_c for all periods.
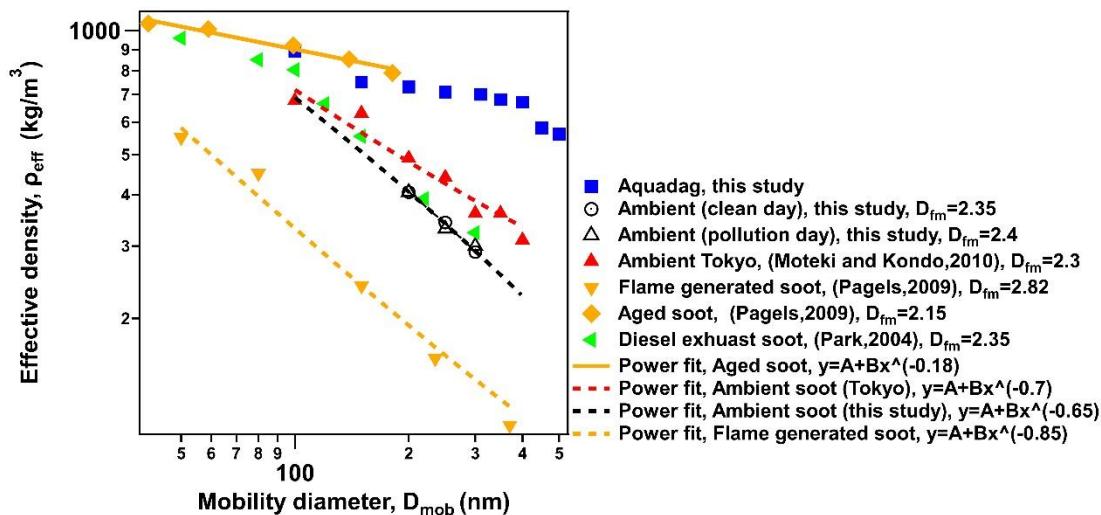
Figure 9. Relationship between effective density and mobility diameter of rBC-containing particles. The black circle and triangle denote the fresh rBC-containing particles ($D_p/D_c = 1$) measured on clean days and polluted days in this study. Other markers denote the data from previous research.
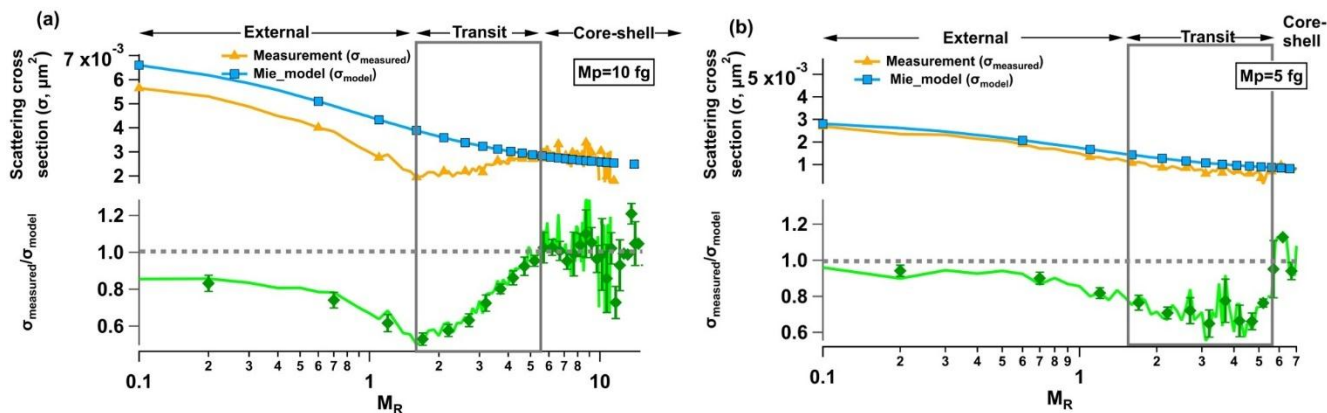
Figure 10. (a) Upper panel: scattering cross section of rBC-containing particles as measured by SP2 (yellow line) and calculated by Mie theory (blue line), assuming a core-shell structure. Bottom panel: the ratio (green line) between these two scattering cross sections at a CPMA setpoint of 10 fg as a function of M_R (the mass ratio of nonrefractory matter to rBC). (b) the same as (a) but for a CPMA setpoint of 5 fg.
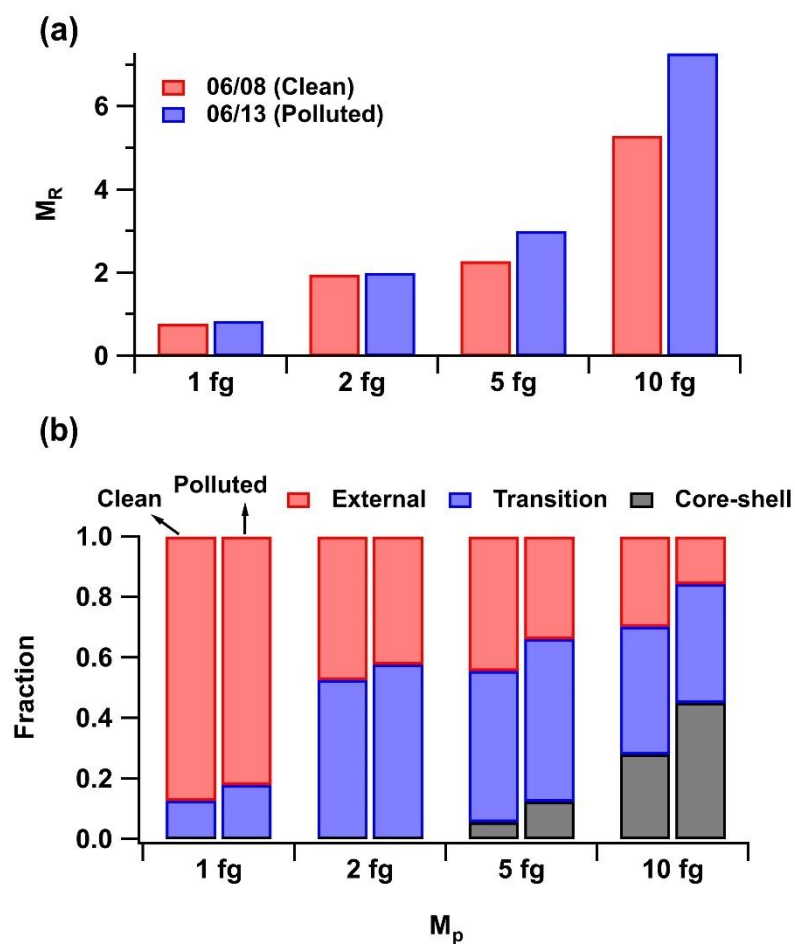
Figure 11. (a) The average M_R (the mass ratio of nonrefractory matter to rBC) under different CPMA setpoints (1 fg, 2 fg, 5 fg, 10 fg). **(b)** The fraction of different types of rBC-containing particles under different CPMA setpoints under varied pollution conditions.

605
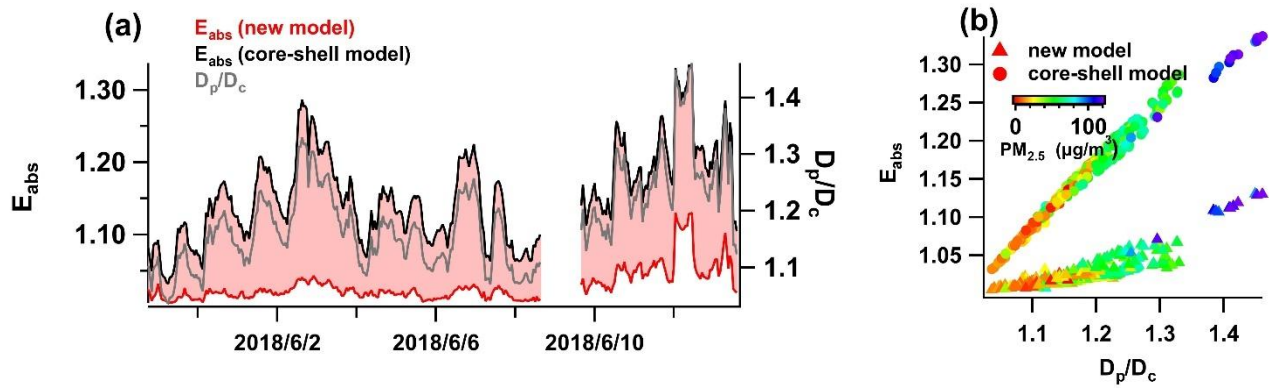
Figure 12. (a) Time series of D_p/D_c with D_c=180±10 nm and E_{abs} at 550 nm wavelength with D_c=180±10 nm using the core-shell model and the morphology-dependent model. **(b)** Relationship between E_{abs} and D_p/D_c. Circles denote the E_{abs} derived from the core-shell model, and triangles denote the E_{abs} derived from the morphology-dependent model.